Thin-Walled Structures 188 (2023) 110794

Contents lists available at ScienceDirect

Thin-Walled Structures

journal homepage: www.elsevier.com/locate/tws

Full length article

Graded honeycombs with high impact resistance through machine learning-based optimization

Yang Gao [a], Xianjia Chen [a], Yujie Wei [a,b,*]

[a] LNM, Institute of Mechanics, Chinese Academy of Sciences, Beijing 100190, China
[b] School of Engineering Sciences, University of Chinese Academy of Sciences, Beijing 100049, China

ARTICLE INFO

Keywords:
Graded honeycomb
Impact resistance
Machine learning
Energy absorption
Equal-load-partition

ABSTRACT

Gradient structures with enhanced performance are ubiquitously observed in nature and in engineering materials. In this paper, we studied the impact resistance of two types of broadly used honeycomb structures (HCSs), a hexagonal HCS and an auxetic HCS. We developed a neural network (NN) which could effectively help to find an optimal gradient design for energy absorption of HCSs in contrast with their uniform counterpart. The optimal density gradient for both hexagonal HCS and auxetic HCS was identified, which are 66% and 40% higher in energy absorption than their respective uniform control. Followed finite-element analysis revealed that density gradient of HCSs enables loading transfer among a greater deformation zone, consequentially more cells involving in energy absorption. The initially graded sample promotes a de-gradient process and leads to more homogeneous density; conversely, a uniform sample develops localized deformation when subject to impact loading. Such an equal-load-partition (ELP) strategy in graded HCSs is responsible for their supreme energy absorption. The developed machine learning (ML) method for impact resistance optimization and the revealed deformation mechanisms in graded HCSs would be meaningful for the design of new advanced graded materials.

1. Introduction

Gradient structures have evolved over millions of years through natural selection and optimization in many biological systems such as bones, horse hooves and plant stems [1], where the microstructures change gradually from the surface to interior. The advantage of gradient structures is to improve a particular property or several ones at stringent material cost. By partially knowing the mechanical environment as a prior, the structure may then be adapted to better its mechanical reliability, and materials bearing such a design motif are now termed as mechanomaterials [2]. Microstructural gradients are increasingly utilized in a wide range of engineering materials for enhanced mechanical properties through an equal-load-partition (ELP) or equal-deformation-partition (EDP) mechanism that is distinct from those operating in their gradient-free counterparts [3–6]. One typical example is functionally gradient coatings (FGCs) with composition [7,8] or structure [9] gradually varying crossing the coating thickness. It was reported that application of FGCs could not only improve the sintering resistance of thermal barrier coatings [9], but also enhance the resistance of protective coatings to contact damages [10–12]. Another important application of gradient strategy is gradient metals. Generally, microstructure gradient of grain size, twin thickness and material composition in metals can be realized through either work hardening (e.g., shot peening [13], surface rolling [14], surface spinning [15], laser shock peening [16]) or phase transformation strengthening (e.g., laser transformation hardening [17], surface carburization [18] and nitridation [19]) in the surface layer, which could not only bring about a negative hardness gradient from surface to interior but also high residual compressive stress near the surface [16,19]. Such microstructural gradient in metals was found able to achieve strength-ductility synergy [20–22], as well as enhanced fracture toughness [4,5], fatigue life [6,23,24] and wear resistance [25,26].

Honeycomb structures (HCSs) have long been used in various impact energy absorbing applications due to their excellent performance and low-density properties [27,28]. Their primary energy absorption mechanism lies in the collapse of cell walls and the plastic deformation undergone, which cannot be significantly improved by merely tuning the geometrical parameters of the composing cells. Inspired by nature, researchers implemented graded design in HCSs by spatially varying the cell wall thickness [29], cell configuration and parameters [30,31], matrix material [32] and hierarchical filling [33], and investigated their energy absorption capacity under diverse loading conditions [30,32,34–36]. When subjected to in-plane impact, the graded HCSs were found to exhibit greater specific energy absorption than

* Corresponding author at: LNM, Institute of Mechanics, Chinese Academy of Sciences, Beijing 100190, China.
E-mail address: yujie_wei@lnm.imech.ac.cn (Y. Wei).

https://doi.org/10.1016/j.tws.2023.110794
Received 26 March 2023; Received in revised form 17 April 2023; Accepted 18 April 2023
Available online 19 May 2023

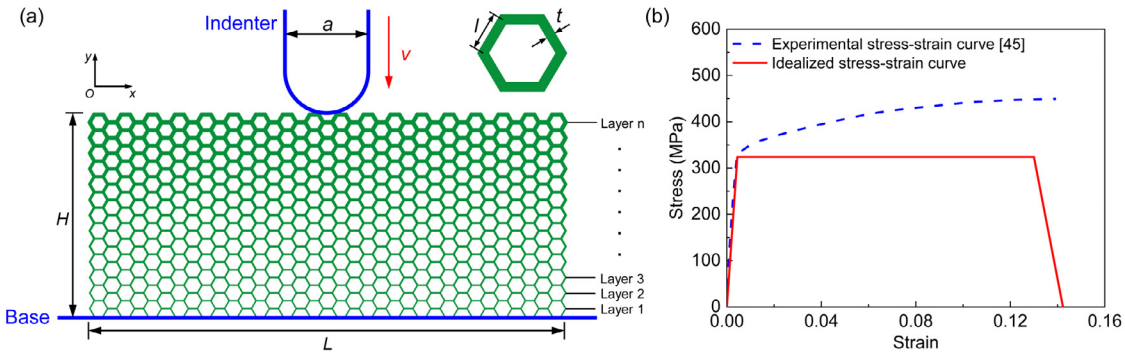

Fig. 1. (a) Schematic diagram showing the quasi three-dimensional graded hexagonal HCS for finite element simulation. Parameters adopted in simulation: $H = 182$ mm, $L = 2040$ mm, $a = 100$ mm, $l = 5$ mm, $t = 1$ mm (uniform control), $v = 5$ m/s. (b) Idealized tensile stress–strain curve of aluminum 2024-T351 walls in a HCS in comparison with the experimental stress–strain curve from Ref. [45].

the uniform ones [37], and such superiority can be attributed to their distinct deformation modes. Current studies are mainly focused on circumstances where the HCSs are subjected to uniform in-plane impact, that is, all honeycomb cells participate in deformation. In many practical engineering applications, however, they serve as buffer components and often carry local impact, under which the deformation in HCS is more complicated. Regardless of studies regarding the deformation in uniform HCSs under local impact [38–40], there remains controversy about the implementation of gradient strategy, e.g., could those structures boost the energy absorption? if yes, is there an optimal gradient design? Zhang et al. [31] investigated the crashworthiness of aluminum foam subjected to local ball impact, and an optimal design of functionally graded foam with maximum crush force efficiency was found, which exhibits 66% higher specific energy absorption over uniform counterpart. In their study, however, the density gradient is only assigned in three layers, implying the explored design space is quite limited. Therefore, the optimal gradient strategy might be of limited reference value for the design of graded HCSs with many more layers.

It is tedious to find the optimal gradient profile in HCSs with multiple layers. The surging of machine learning (ML) in scientific discoveries seems to offer a solution to this problem at low cost [41–44]. Through the method of ML, for instance, Wan et al. [41] found the optimal hole distribution in graphene with minimum thermal conductivity; Gu et al. [42] obtained the optimal distribution of hard and soft phases in composites for maximum strength and toughness. In this study, we investigate the impact resistance of graded HCSs under local impact, and search for optimal gradient in HCSs for highest impact resistance via ML technique, aiming to provide guideline for the design of graded cellular materials. Two types of broadly used HCSs, i.e., conventional hexagonal HCS and re-entrant auxetic HCS, were studied, mainly because of their distinction in Poisson's ratio, with positive value for the former and negative for the latter.

2. Conventional hexagonal HCS

We start with the conventional hexagonal HCS with positive Poisson's ratio. Different from aforementioned coatings and metallic materials whose compositional or structural gradient is technically challenging to be finely tuned for property optimization, the density gradient in HCSs can be well regulated layer by layer. Given the large design space of graded HCSs, exhaustive FE calculations to find an optimal profile are computationally prohibitive. To the contrary, ML with a few numbers of computational samples may dramatically expedite the searching process.

Table 1
Properties of aluminum alloy 2024-T351 adopted in simulation.

Property	Value
Density/(kg/m^3)	2780 [48]
Elastic modulus/GPa	73.1 [48]
Poisson's ratio	0.33 [48]
Yield strength/MPa	324 [48]
Fracture strain (Stress-triaxiality dependent)	0.08–0.6 [46]
Fracture energy	2 mJ/mm^3

2.1. Dataset generation

To evaluate the effect of graded density on the impact resistance of hexagonal HCS, finite element simulations are performed with commercial FEA package ABAQUS (Version 6.14, Dassault Systèmes, France). As schematically shown in Fig. 1(a), the simulating parts are composed of the hexagonal HCS, up indenter and bottom base. The indenter and base are both assumed to be rigid materials. The constituent material employed for HCS is a typical aluminum alloy 2024-T351, which is assumed to be elastic-perfectly-plastic in our simulation and whose properties are listed in Table 1. A ductile damage model is adopted to capture cell-wall failure. The equivalent plastic strain at the onset of damage is assumed to be stress-triaxiality dependent with values adopted from literature [46]. Given the low strain-rate sensitivity of aluminum alloy [47] within the strain-rate range of interest, we neglect its rate-sensitivity. To model the damage evolution, the energy with linear softening law is chosen and a failure energy 2 mJ/mm^3 is used. Fig. 1(b) gives its uniaxial tensile stress–strain curve employed in simulation in comparison with the experimental curve.

The height and length of HCS are taken as $H = 182$ mm and $L = 2040$ mm, corresponding to 21 and 272 cells in the vertical and longitudinal directions, respectively. To reduce calculation costs, the out-of-plane width of HCS is taken as 1 mm. The indenter has a semi-circular tip with a diameter $a = 100$ mm, which is 20 times of the cell wall length l ($l = 5$ mm) to avoid over-localized deformation. Shell element (S4R) is adopted to simulate the HCS. For uniform hexagonal HCS, its density ρ^* relative to that of its fully dense counterpart ρ_s is given as [49]: $\frac{\rho^*}{\rho_s} = \frac{2}{\sqrt{3}}\frac{t}{l}\left(1 - \frac{1}{2\sqrt{3}}\frac{t}{l}\right)$. For samples with equal thickness $t = 1$ mm and $l = 5$ mm, $\frac{\rho^*}{\rho_s} = 0.218$. In simulation, the vertical degree of freedom of HCS is fixed on the bottom, and periodic boundary condition is applied on its lateral sides. The out-of-plane deformation of HCS is constrained to simulate the plane-strain condition. The friction between the indenter tip and the material is considered by assigning a constant friction coefficient 0.3. Penetration between collapsed cell walls is prohibited by assuming hard contact, and their relative sliding follows a friction law with a friction coefficient of 0.3. A constant velocity of 5 m/s is applied to the indenter along the vertical direction for a time of 0.03 s (150 mm in displacement). Then the total energy

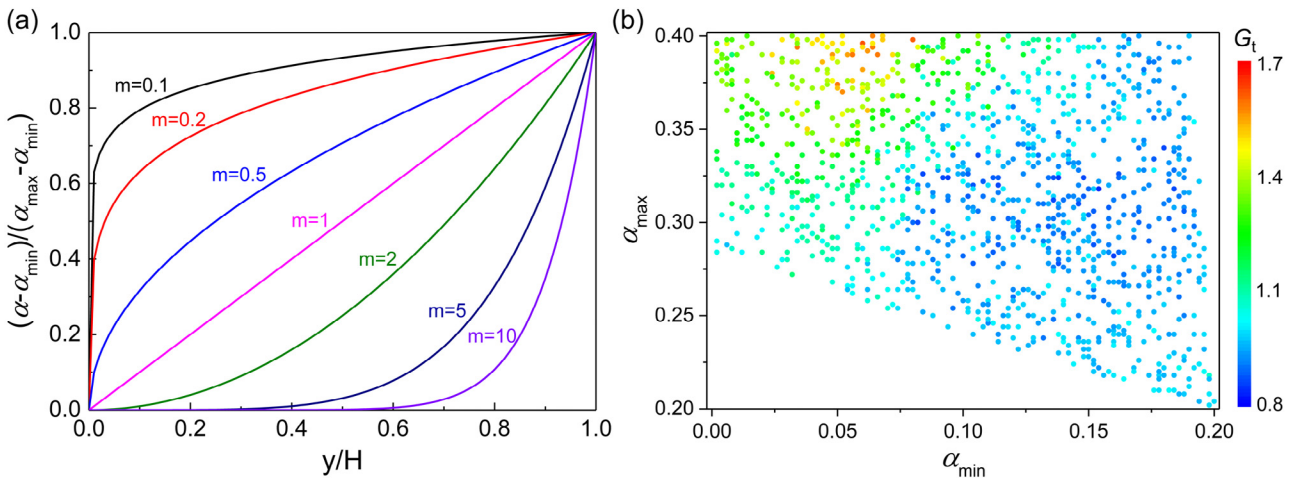

Fig. 2. (a) The variation of cell wall aspect ratio along vertical direction in power law for different m. (b) Calculated energy absorption capability of randomly selected 1100 graded samples. Here, their energy absorption capability is normalized by that of the uniform control.

absorbed by HCS can be obtained by calculating the area below the indenter's force–displacement curve.

By contrast, the graded hexagonal HCSs are constructed by assigning different thickness to the shell element layer by layer (see Fig. 1(a)) while keeping its total mass equal to that of the uniform counterpart. In practical applications, the impact-resistant components might not only subject to impact loading but also loadings of other modes, and it would be safer to place a stiffer layer outside. This might somewhat explain why the density in many biological materials is decreased from surface to interior [1]. In this study, therefore, we focus on the negative graded HCS with relative density decreased from impact end to fixed end. Since the relative density of hexagonal HCS (ρ^*/ρ_s) is roughly proportional to the aspect ratio of $\alpha = t/l$, the density gradient is then characterized by α. For simplicity, we assume the ratio α of graded HCS decreases monotonically from the impact end to the fixed end in the form of (see Fig. 2(a)):

$$\alpha\left(\frac{y}{H}\right) = \alpha_{\min} + \left(\alpha_{\max} - \alpha_{\min}\right)\left(\frac{y}{H}\right)^m \left(0 \le y \le H\right) \tag{1}$$

in which $\alpha_{\min}$ and $\alpha_{\max}$ represent the aspect ratio of cell wall on the fixed end and impact end, respectively, and m is a power index. Given that its total mass is constant, the index m can be solved uniquely from Eq. (1) with known $\alpha_{\min}$ and $\alpha_{\max}$. Therefore, in the dataset for ML, $\alpha_{\min}$ and $\alpha_{\max}$ of the graded HCS will be taken as inputs while the total energy absorption (G) as output. The parameter space of the input variables is defined as $\alpha_{\min} \in (0, 0.2]$, $\alpha_{\max} \in (0.2, 0.4]$. The total mass of the graded HCS is equal to that of the uniform control when $\alpha = 0.2$.

To fully explore the parameter space of input variables, a grid-search strategy is adopted to generate the dataset for ML. Each input domain is discretized into n_i uniform intervals and a grid of all possible input variables is then constructed inside the parameter space. This gives rise to $N = \left(1+n_1\right)\left(1+n_2\right)\ldots\left(1+n_i\right)$ different samples. In this study, the intervals of the two input variables are taken as 0.002, thus yielding a total number of 10^4 samples. For some combinations of $\alpha_{\min}$ and $\alpha_{\max}$, however, solving Eq. (1) for index m cannot produce a real number, which would be excluded from the dataset. Finally, 7720 available combinations of $\alpha_{\min}$ and $\alpha_{\max}$ are attained for the input dataset. To save calculation costs, we randomly shuffle the 7720 samples in the dataset and select 1100 samples (see Fig. 2(b)) from them. Finite element analysis is performed to evaluate the energy absorption of the 1100 samples, as shown in Fig. 2(b), which will be taken as training data for subsequence ML. The energy absorption of graded HCSs mentioned in this study is all normalized by that of the uniform control.

2.2. NN model training

By using the dataset generated last subsection, a NN model will be trained to predict the energy absorption of graded HCSs in the context of supervised learning. The dataset (1100 samples) is split into training dataset (70%), validation dataset (20%), and test dataset (10%). The validation dataset is used to find better architectures, and the test dataset is used to assess the model performance. The goal of the parameter optimization is to minimize the root mean square error (RMSE) between the predictions and targets with Adam optimizer:

$$\mathrm{RMSE} = \sqrt{\sum_{i=1}^{n} \frac{\left(G_t^i - G_p^i\right)^2}{n}} \tag{2}$$

in which n is the number of data, and for the ith sample, G_t^i and G_p^i are the true energy absorption from FE simulation and the predicted one by NN model, respectively. We also introduce the following quantity (R^2) to measure the quality of the regression performance of the model as

$$R^2 = 1 - \frac{\sum_{i=1}^{n}\left|G_t^i - G_p^i\right|^2}{\sum_{i=1}^{n}\left|G_t^i - \frac{1}{n}\sum_{i=1}^{n} G_t^i\right|^2} \tag{3}$$

During the tuning, a learning rate of 0.0001 is chosen for the optimizer with a batch size of 10 and the number of maximum epochs is set 5000. A NN model with two hidden layers (2/25/25/1) is found to achieve $R^2 = 0.92$ on the test dataset, indicating that the trained NN model can extract major features of graded HCSs and accurately predict their energy absorption performance.

2.3. Inverse design

Based on the developed NN model, we will present an inverse design scheme [41,43,50] to search for the graded HCS with maximum impact resistance. As shown in Fig. 3, at first, we randomly select 100 samples from the library of all possible structures (7720) and calculate their energy absorption using FE simulation, which are taken as training data. The NN model is trained by the train set as the first generation NN model, which is then used to predict the energy absorption of all the remaining samples in the library. Based on both the NN-predicted data and the calculated training data, the top 100 graded structures of all possibilities can be found. For the top 100 structures that are not included in the training set, their true energy absorption is computed by FE simulations. The data of these newly calculated structures is then added to the training set, and the extended training set is used

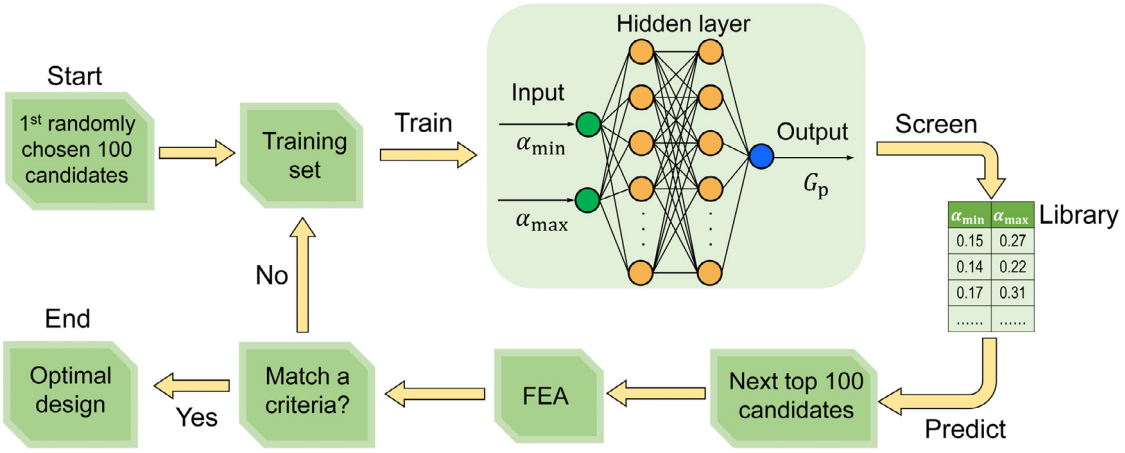

Fig. 3. Schematic of NN model-based search algorithm.

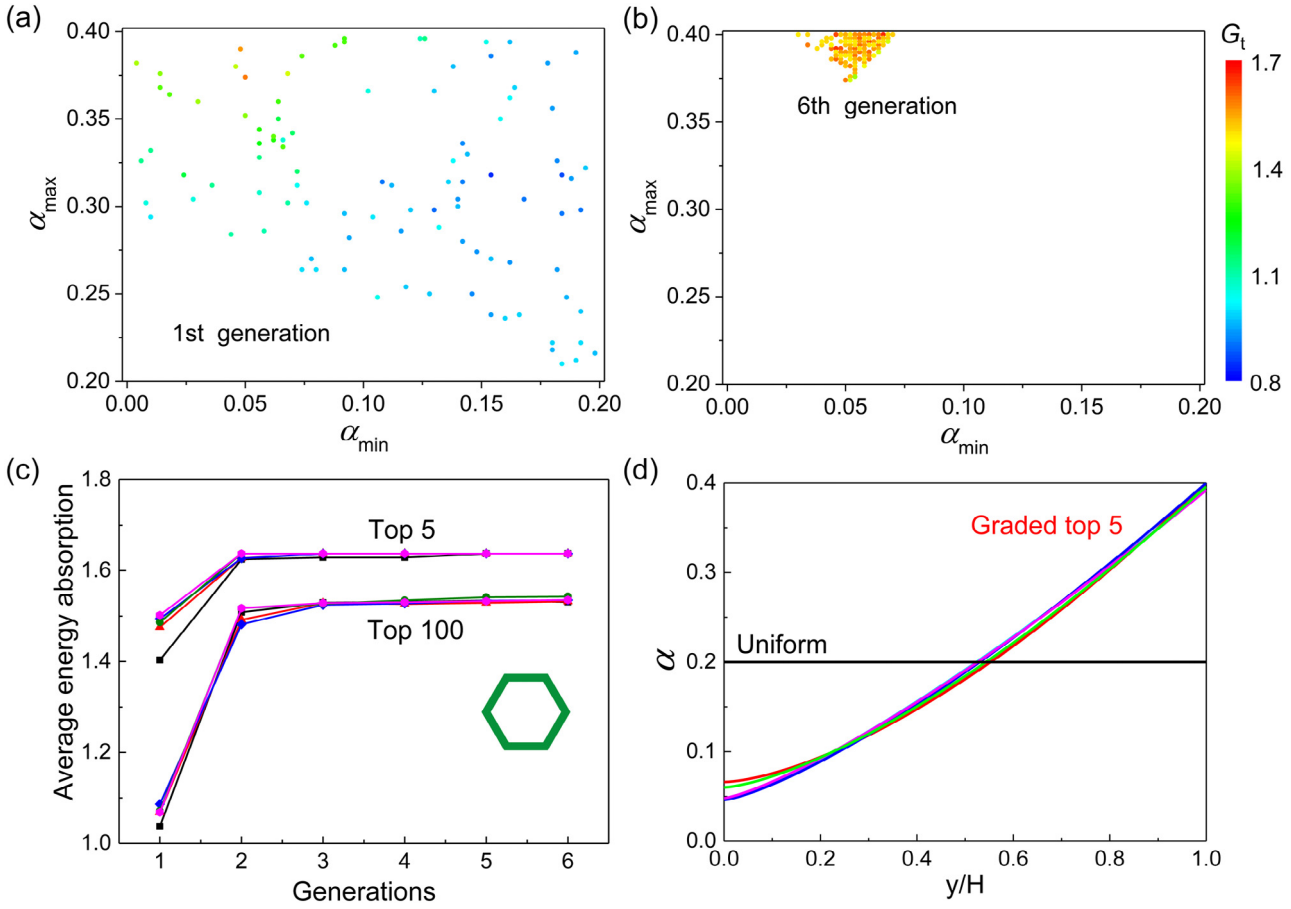

Fig. 4. Searching for optimal graded hexagonal HCSs via inverse design. (a) Initial training dataset (100 samples) for one typical searching process, and (b) corresponding top 100 performers in the 6th generation. (c) Average energy absorption of the top 100 and top 5 performers as a function of searching generations. The energy absorption of graded HCSs is normalized by that of the uniform counterpart. (d) The relative density distribution of the ML-searched top 5 graded hexagonal HCSs.

to train the next-generation NN model. To evaluate the performance of the search scheme, we use the average energy absorption of the top 100 structures in the extended training set of each generation as the convergence measurement. It should be noted that in the searching process, the size of the training set increases gradually with iteration. In each generation of the inverse design process, the NN model is initialized at first and then trained based on the training set to predict the energy absorption of the remaining samples. To demonstrate the effectiveness of this search scheme, this searching process is repeated multiple times by choosing totally different initial training data.

Fig. 4(a) and (b) display the initial training data of one typical searching process and corresponding top 100 performers in the 6th generation, respectively. Clearly, even starting with randomly dispersed data points, structures with supreme performance can be well found through such search algorithm. Fig. 4(c) shows the variation of the average energy absorption of the top 100 and top 5 structures in the training set with searching generations. Here, the searching process is repeated 5 times with totally different initial training data, which are represented by distinct colored lines. As can be seen, regardless of the initial training dataset, the average energy absorption of the top 100

structures converges quickly to the same level (around 1.5 times of that of uniform control), affirming the effectiveness of the inverse design search algorithm. In the 6th generation, the same top 5 performers are found (see Fig. 4(c)), which exhibit similar gradient in density (see Fig. 4(d)). That is, the aspect ratio of cell wall on the impact end (α_{max}) is around 0.4, which is the upper limit assumed in this study, while around 0.05 on the fixed end (α_{min}). Here, the demand for ultra-high density on the impact end is associated with the deformation mechanism of graded hexagonal HCSs, which will be elaborated in the following.

We next take a closer look at the deformation mechanism of the ML-explored optimal performer. Fig. 5 presents the computed force–displacement curves of the optimal graded HCS and the uniform control, in company with the snapshots showing their deformation evolutions. For both of them, three characteristic deformation stages, i.e., elastic stage, plateau stage and densification stage, can be clearly identified in their stress–strain curves (see Fig. 5(a)). By calculating the area below the force–displacement curve with displacement ranging from 0 to 150 mm, which well covers the region before densification, the optimal structure is found to exhibit 66% improvement in energy absorption than the uniform control. Despite significant enhancement in energy absorption, its crashing force is maintained at a roughly steady level in the plateau stage with peak crashing force increased by 77% (see Fig. 5(a)), which is roughly proportional with the improvement in energy absorption. Such superiority over gradient-free counterpart can be ascribed to their distinct deformation mechanisms. For the uniform HCS, as illustrated in Fig. 5(b), only the cells in direct contact with indenter are gradually collapsed and fractured as impact proceeds, during which the initially uniform sample develops localized deformation with high density gradient (see Fig. 5(c)). By contrast, for the optimized graded HCS, the locally applied loading could be transferred over a larger deformation zone (see Fig. 5(d)), thus facilitating more energy absorption. As opposed to the uniform control, this is a de-gradient process and the density distribution becomes more uniform as deformation proceeds (see Fig. 5(e)). Such an ELP strategy in graded HCSs is considered responsible for their supreme energy absorption.

Since the superiority of graded HCSs primarily arises from the extra cell deformation and collapse beyond the impact trajectory that occur near the fixed end, one should cause as much energy absorption near the fixed end as possible for high impact resistance. When the structural density near the fixed end is ultra-low, large-scale cell collapse cannot absorb much energy. For higher energy absorption, therefore, the density on the fixed end should be increased. At the same time, the density on the impact end should be increased synergistically to ensure that it is stiff enough to trigger large-scale cell collapse near the fixed end. Then the maximum energy absorption can be realized when either the minimum density on the fixed end (α_{min}) or the maximum density on the impact end (α_{max}) increases to its upper limit. This may explain the demand for ultra-high density (upper limit) on the impact end of the optimized graded hexagonal HCS.

3. Re-entrant auxetic HCS

Above section demonstrates the effectiveness of graded design on amplifying the impact resistance of conventional hexagonal HCSs. In the following, our study will be extended to re-entrant HCSs with negative Poisson's ratio.

3.1. Dataset generation

Likewise, finite element simulations are carried out to evaluate the effect of graded density on the impact resistance of re-entrant HCSs. Here, except for the HCS, the finite element model employed for simulation is identical to that of last section. As shown in Fig. 6, the overall height and length of HCS are taken as $H = 182$ mm and $L = 2040$ mm, corresponding to 21 and 227 cells in the vertical and longitudinal directions respectively, and its out-of-plane width is taken as 1 mm to save calculation costs. For the re-entrant unit cell, the horizontal and inclined lengths are taken as $h = 7$ mm and $l = 5$ mm, respectively, with cell angle $\theta = 60°$. For the uniform structure, equal cell wall thickness is assigned to each layer as $t = 0.7$ mm, with relative density calculated as [51]: $\frac{\rho^*}{\rho_s} = \frac{t/l(h/l+2)}{2\sin\theta(h/l-\cos\theta)} \approx 0.305$. The graded HCSs are constructed by assigning different thickness to the shell element layer by layer (see Fig. 6) while keeping the total mass identical to that of the uniform control. Here, the gradient in the aspect ratio of cell wall ($\alpha = t/l$) is used to depict the density gradient in re-entrant HCSs, which is assumed to follow the power law (see Eq. (1) and Fig. 2(a)). The parameter space of the input variables is defined as $\alpha_{min} \in (0, 0.14]$, $\alpha_{max} \in (0.14, 0.24]$. Here, the upper bound for α_{max} sets the high end of HCS's density to be around 52%. The total mass of the graded HCS is equal to that of the uniform control with $\alpha = 0.14$. Taking the intervals of the two input variables as 0.002, a total number of 2459 combinations of α_{min} and α_{max} for the input dataset can be found. It should be mentioned that, due to the high relative density of re-entrant HCSs and resultant earlier densification, the impact displacement for calculating the energy absorption of re-entrant HCSs is shortened to 140 mm.

3.2. NN model training

In general, different ML models should be trained for different problems due to their distinct mapping relationships between inputs and outputs. However, it usually takes vast computation and time resources to train a new model. As a matter of fact, a model specifically-developed for one problem can be applied to solve other problems of some similarities with high efficiency [52], which is termed as transfer learning [53]. Considering the structural similarity between the hexagonal and re-entrant HCSs in this study (21 layers along the vertical direction and constrained out-of-plane deformation), we will now apply the NN model with two hidden layers (2/25/25/1) developed in last section to search for the optimal graded re-entrant HCS.

3.3. Inverse design

By using the NN model, we explored the optimal graded re-entrant HCS based on the search algorithm shown in Fig. 3. Fig. 7(a) and (b) display the initial training dataset for one typical searching process and the corresponding top 100 performers in the 6th generation, respectively. With the increase of searching generations, the average energy absorption of top 100 performers converges quickly to the same level (around 1.3 times of that of the uniform control) despite completely different initial training datasets in different searching processes, as shown in Fig. 7(c), demonstrating the effectiveness of the searching algorithm. Additionally, in the 6th generation, the same top 5 designs are found (see Fig. 7(c)), which share similar density gradient (see Fig. 7(d)). Specifically, the aspect ratio of cell wall on the impact end (α_{max}) is around 0.21, while approaching zero (the lower limit assumed in this study) on the fixed end (α_{min}). The requirement for ultra-low density on the fixed end arises from its deformation mechanism, which will be explained below.

Fig. 8(a) presents the force–displacement curve of the optimized graded re-entrant HCS, and an overwhelming advantage over the uniform control can be observed. In contrast with a steady stress level for the uniform counterpart, an ever-increasing stress is observed in the plateau deformation stage of the optimized graded HCS. By calculating the area below the force–displacement curve with displacement ranging from 0 to 140 mm, the energy absorption of the graded HCS is found around 40% higher than that of the uniform control, while accompanied with the increment of peak crashing force by more than 100%. Apparently, by enlarging the impact distance, more extra energy consumption can be realized at the expense of even higher peak crashing

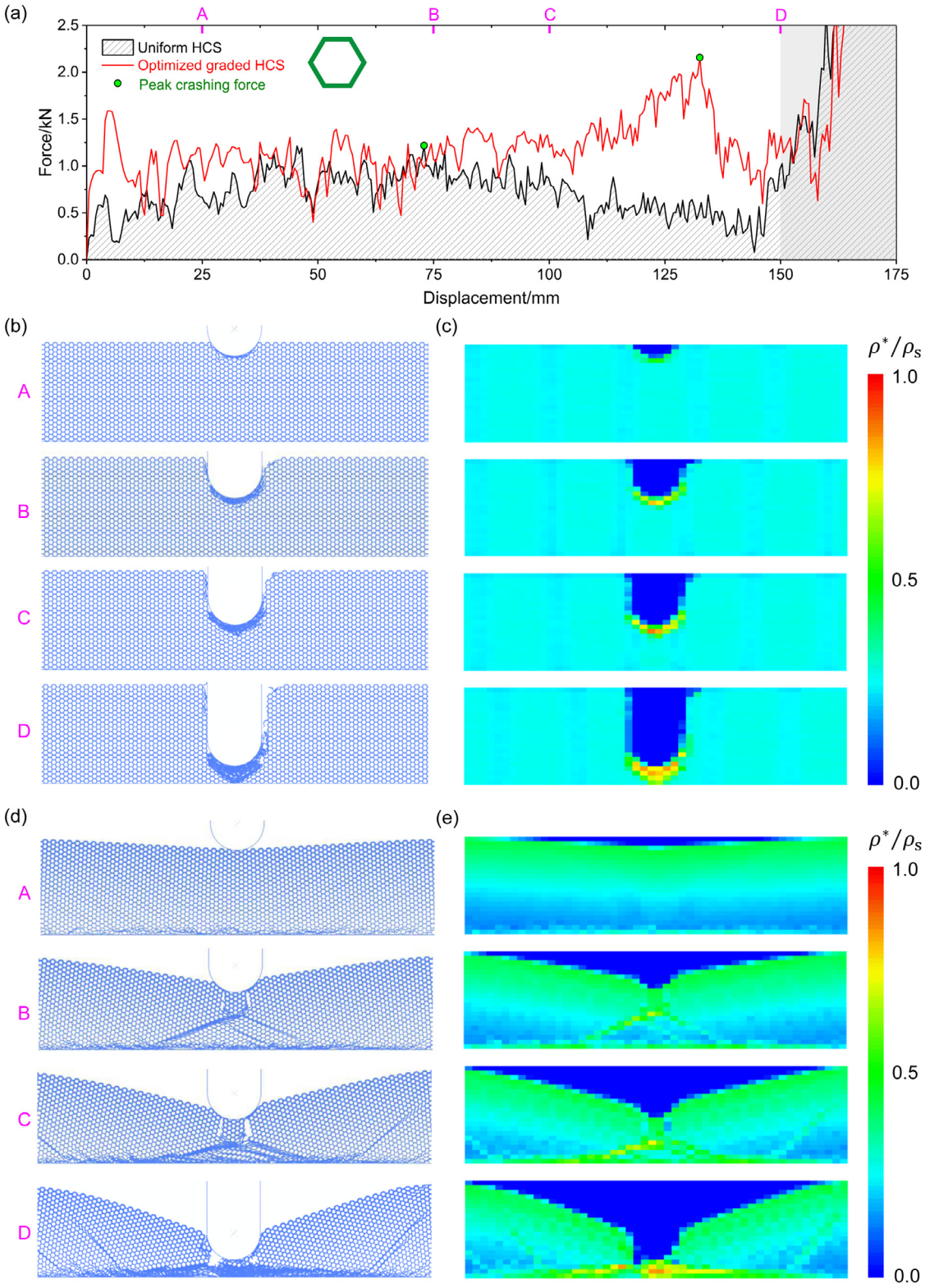

Fig. 5. FEM simulations to show the impact resistance of hexagonal HCS. (a) Force–displacement curves of the optimized graded HCS and the uniform control. Snapshots showing (b, d) the deformation evolution and (c, e) corresponding relative density distribution in (b, c) uniform and (d, e) optimized graded HCSs at different loading moments (denoted as A-D as indicated in (a)). For clarity, cells far from the deformation zone are not shown in (b-e).

force. To account for such superiority, their deformation mechanisms are further examined. For the uniform re-entrant HCS, the re-entrant cells in contact with the indenter are gradually collapsed and fractured as deformation proceeds. Meanwhile, the neighboring cells surrounding the indenter contract laterally due to the negative Poisson's ratio (see Fig. 8(b)). The deformation process of the optimized graded HCS is depicted in Fig. 8(d). At early deformation stage, the weak cells on the fixed end are firstly collapsed on a large scale, followed by cell collapse near the impact end ('A' in Fig. 8(d)). As deformation proceeds, re-entrant cells near the fixed end and impact end collapse simultaneously

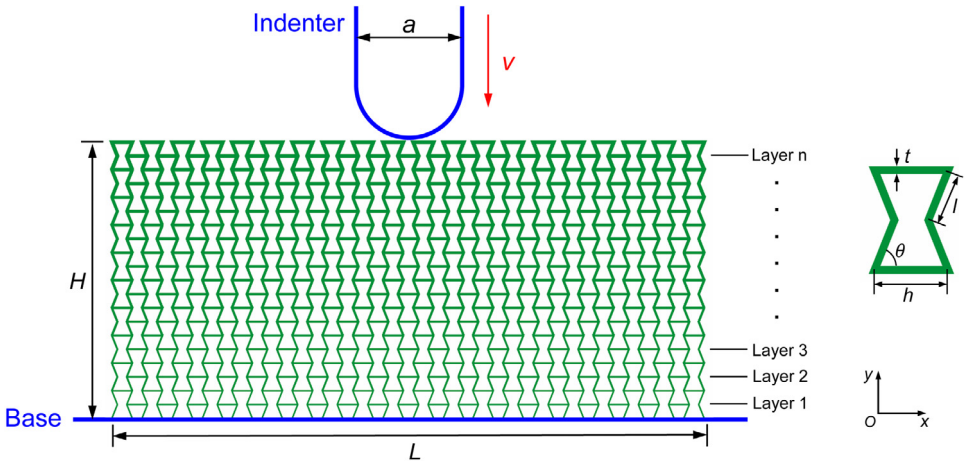

Fig. 6. Schematic diagram showing the quasi three-dimensional graded re-entrant HCS for impact simulation. Parameters adopted in simulation: H = 182 mm, L = 2040 mm, a = 100 mm, l = 5 mm, h = 7 mm, $\theta = 60°$, t = 0.7 mm (uniform control), v = 5 m/s.

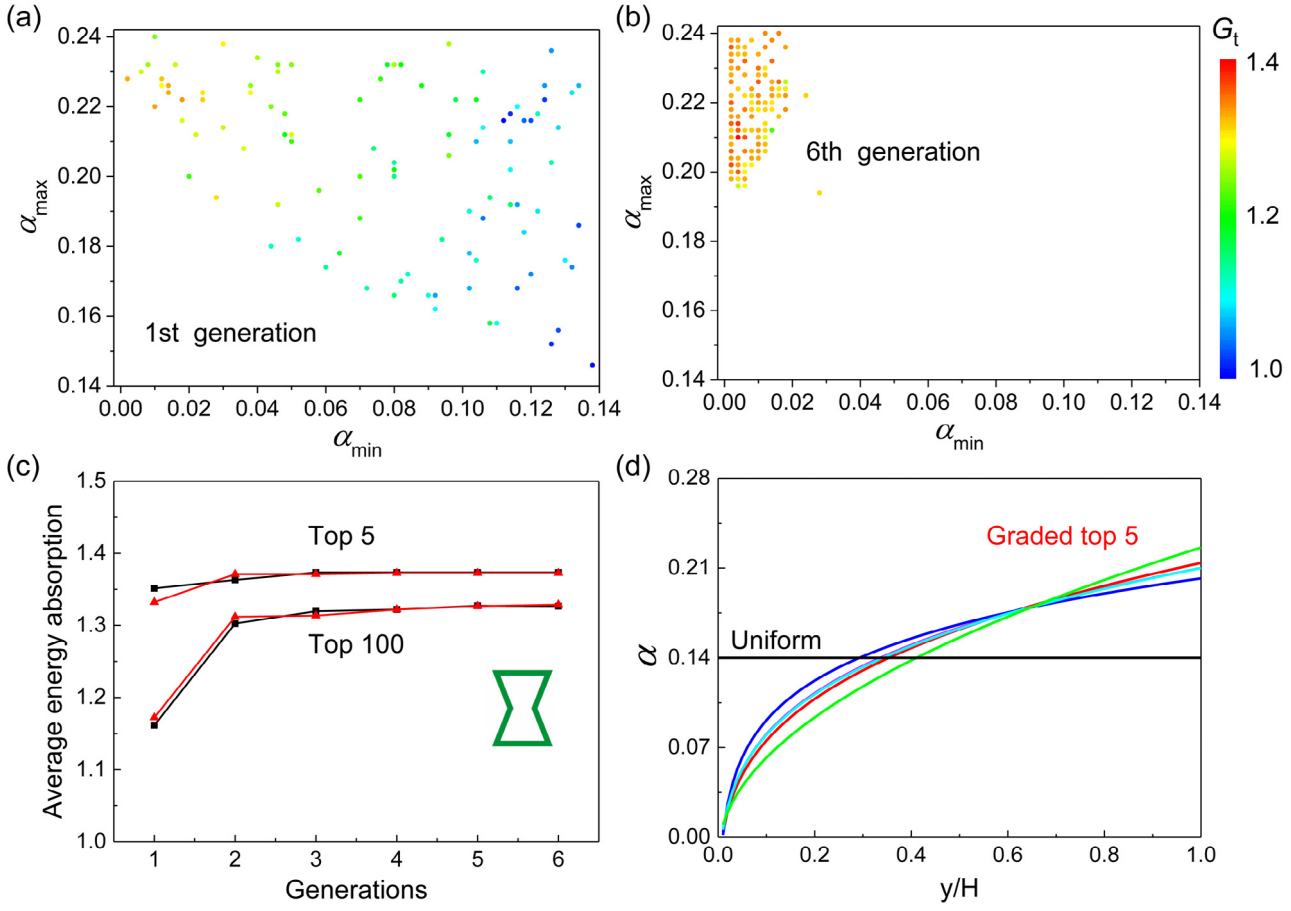

Fig. 7. Searching for optimal graded re-entrant HCSs via inverse design. (a) Initial training dataset (100 samples) for one typical searching process, and (b) corresponding top 100 performers in the 6th generation. (c) Average energy absorption of the top 100 and top 5 performers as a function of searching generations. The energy absorption is normalized by that of the uniform counterpart. Here, the searching process is repeated twice with totally different initial training data, which are represented by different colored lines for distinction. (d) The relative density distribution of the ML-searched top 5 graded samples.

('B' in Fig. 8(d)). Meanwhile, the compressed cells could contract laterally before complete densification owing to the auxetic effect, thus densifying the structure well below the indenter and yielding higher crashing force. During this stage (from 'A' to 'C' in Fig. 8(a)), the advantage of graded HCS is fully demonstrated. As opposed to the development of high density gradient in the initially uniform HCS (see Fig. 8(c)), the graded re-entrant HCS could facilitate gradient elimination and lead to a more homogeneous density distribution (see Fig. 8(e)). This contributes to ELP in graded HCSs for supreme energy absorption.

The reinforcing mechanism of density gradient in re-entrant HCSs can be summarized in two aspects. On the one hand, negative density gradient enables loading transfer over a larger deformation zone, thereby more cells involved in energy absorption. On the other hand, early deformed cells due to density gradient can shrink laterally before complete densification, thus yielding higher structural density below

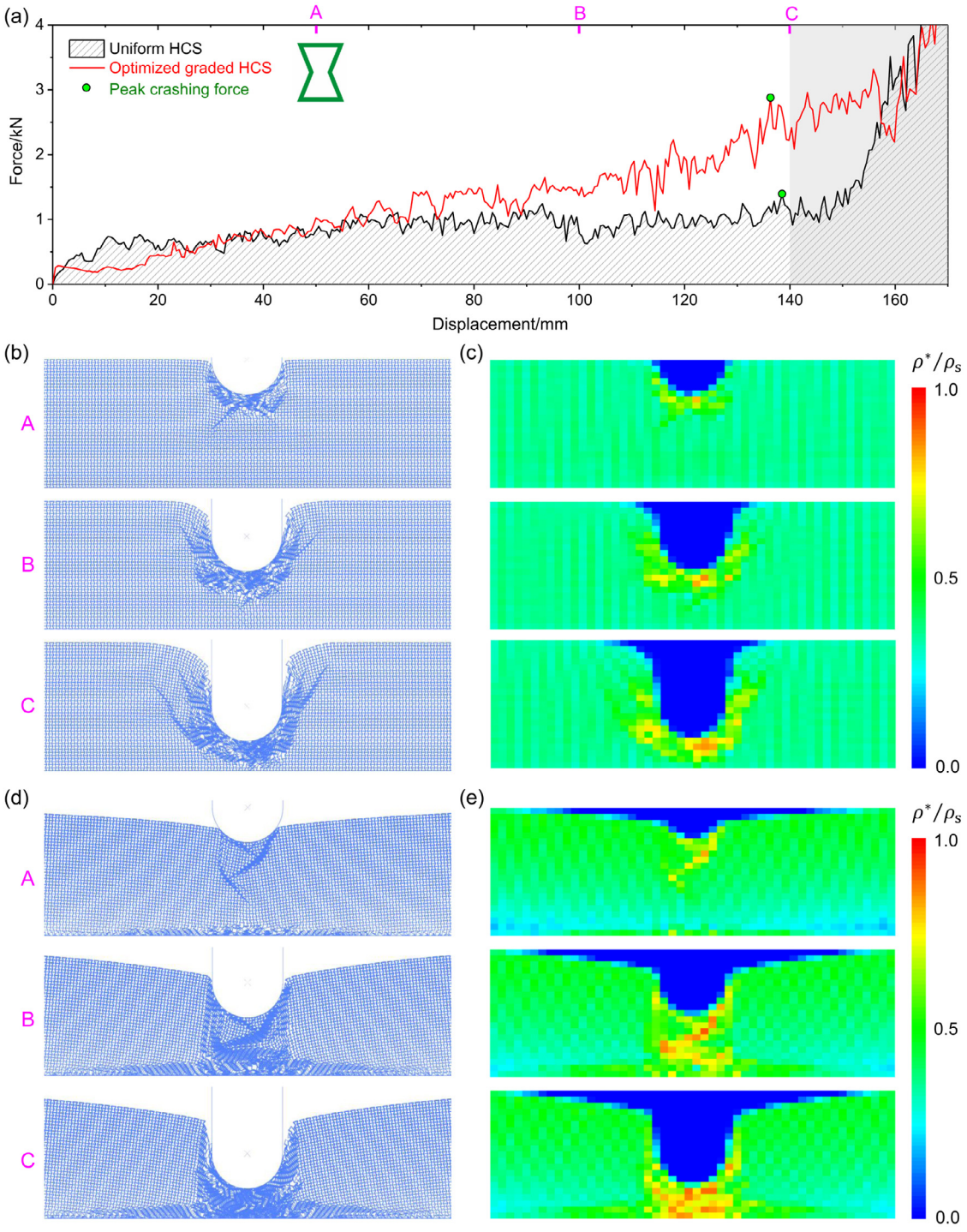

Fig. 8. FEM simulations to show the impact resistance of re-entrant HCS. (a) Force–displacement curves of the optimal graded sample and its uniform control. Snapshots showing (b, d) the deformation evolution and (c, e) corresponding relative density distribution in (b, c) uniform and (d, e) optimized graded HCSs at different loading moments (denoted as A-C as indicated in (a)). For clarity, cells far from the deformation zone are not shown in (b-e).

the indenter and therefore higher crashing force. The optimization of density gradient is to modulate the cooperation of the two mechanisms to maximize its overall performance on energy absorption. Clearly, the ML-searched optimal design with ultra-low density near the fixed end enables the latter one to play a dominant role, and such allocation may be dependent on the height (H) of a re-entrant HCS.

4. Discussion and conclusion

In search for the optimal density gradient by inverse design, the initial training dataset (100 samples) is randomly selected from the whole library, which may somewhat represent the average impact-resistance performance of all available samples. The average energy absorption of the initial training data is around 1.05 times (see Fig. 4(c)) of the uniform control for hexagonal HCSs, while 1.15 times (see Fig. 7(c)) for re-entrant HCSs. Such contrast suggests that the implementation of gradient strategy in re-entrant HCSs is more effective in improving the impact resistance. This can be further confirmed by comparing Fig. 4(a) (or Fig. 2(b)) and Fig. 7(a). As can be seen, a large portion of graded hexagonal HCSs underperform their uniform control, while almost all graded re-entrant designs outperform their uniform counterpart. Therefore, in some less-demanding conditions, it may not necessary to cost

too much efforts to optimize the density gradient in re-entrant HCSs for maximum energy absorption, while a randomly determined gradient profile might be able to bring about great extra energy consumption. However, this is often accompanied by high peak crashing force, which is often unfavorable since it might cause damage to the objects they protect. In some conditions that require for both high energy absorption and low crashing force, the graded hexagonal HCS is a better choice, whose density gradient needs to be well optimized before use.

Although the impact resistance of graded HCSs has been largely improved through structural optimization, limitations remain present in our work. Firstly, to simplify the optimization process by ML, the density of graded HCS was assumed to decrease monotonically following the power law, while the true optimal density gradient might not necessarily follow the power law exactly. In addition, some biological materials, such as the stomatopod dactyl club that is well-known for high damage-tolerance [54], were found to exhibit periodic gradient stiffness distribution, which was demonstrated to be much superior than uniform control in terms of impact resistance [55]. This inspires us to upgrade the present monotonic density gradient in HCSs to periodic ones for higher impact resistance. On the other hand, the indenter size (a) and the characteristic length of the honeycomb structure (H) were both assumed to be constant in this work. Further studies are required to shed light on the dependence of the optimal gradient profile and the corresponding energy absorption capability on the ratio H/a. Lastly, we focused on the deformation of HCSs under low-velocity (quasi-static) impact. It has been demonstrated that mechanical behavior of HCSs under impact are highly dependent on the impact velocity [38,56–58]. Further investigations are needed to take velocity as a factor for structure optimization.

In summary, we investigated the impact resistance of two types of HCSs, hexagonal HCS and re-entrant HCS. To find the optimal gradient design in HCSs with highest impact resistance, ML was used to approximate the energy absorption capability as a function of density gradient. A straightforward NN model was found able to effectively predict the energy absorption of graded HCSs. By incorporating the inverse design algorithm and ML technique, the optimal graded HCSs were found for both hexagonal HCS and re-entrant HCS, whose energy absorption is 66% and 40% higher than that of their respective uniform control. Such superiority of graded HCSs can be attributed to the ELP deformation strategy, which enables loading transfer over a larger deformation zone, thus more cells are involved in energy absorption. Our work not only demonstrates the effectiveness of ML approach to find the optimal graded HCSs with high impact resistance, but also reveals the deformation mechanisms of graded HCSs responsible for such exceptional performance.

CRediT authorship contribution statement

Yang Gao: Writing – original draft, Software, Methodology, Investigation. **Xianjia Chen:** Software, Methodology. **Yujie Wei:** Writing – review & editing, Supervision, Resources, Project administration, Funding acquisition, Conceptualization.

Declaration of competing interest

The authors declare that they have no known competing financial interests or personal relationships that could have appeared to influence the work reported in this paper.

Data availability

Data will be made available on request.

Acknowledgments

Y.W. acknowledges support from the NSFC Basic Science Center, China for “Multiscale 6 Problems in Nonlinear Mechanics” (No. 11988102). Y.G. thanks support from NSFC, China (No. 12202447) and China Postdoctoral Science Foundation, China (No. 2021M703289).

References

[1] Z. Liu, M.A. Meyers, Z. Zhang, R.O. Ritchie, Functional gradients and heterogeneities in biological materials: Design principles, functions, and bioinspired applications, Prog. Mater. Sci. 88 (2017) 467–498.
[2] P. Cai, C. Wang, H. Gao, X. Chen, Mechanomaterials: A rational deployment of forces and geometries in programming functional materials, Adv. Mater. (2021) 2007977.
[3] Y. Gao, H. Yao, Homogenizing interfacial shear stress via thickness gradient, J. Mech. Phys. Solids 131 (2019) 112–124.
[4] R. Cao, Q. Yu, J. Pan, Y. Lin, A. Sweet, Y. Li, R.O. Ritchie, On the exceptional damage-tolerance of gradient metallic materials, Mater. Today 32 (2020) 94–107.
[5] Y. Lin, Q. Yu, J. Pan, F. Duan, R.O. Ritchie, Y. Li, On the impact toughness of gradient-structured metals, Acta Mater. 193 (2020) 125–137.
[6] Z. Ma, J. Liu, G. Wang, H. Wang, Y. Wei, H. Gao, Strength gradient enhances fatigue resistance of steels, Sci. Rep. 6 (1) (2016) 1–11.
[7] X. Chen, L. Gu, B. Zou, Y. Wang, X. Cao, New functionally graded thermal barrier coating system based on LaMgAl11O19/YSZ prepared by air plasma spraying, Surf. Coat. Technol. 206 (8–9) (2012) 2265–2274.
[8] P. Carpio, E. Bannier, M. Salvador, R. Benavente, E. Sánchez, Multilayer and particle size-graded YSZ coatings obtained by plasma spraying of micro-and nanostructured feedstocks, J. Therm. Spray Technol. 23 (8) (2014) 1362–1372.
[9] B. Lv, X. Fan, D. Li, T. Wang, Towards enhanced sintering resistance: Air-plasma-sprayed thermal barrier coating system with porosity gradient, J. Eur. Ceram. Soc. 38 (4) (2018) 1946–1956.
[10] J. Jitcharoen, N.P. Padture, A.E. Giannakopoulos, S. Suresh, Hertzian-crack suppression in ceramics with elastic-modulus-graded surfaces, J. Am. Ceram. Soc. 81 (9) (1998) 2301–2308.
[11] D. Pender, N. Padture, A. Giannakopoulos, S. Suresh, Gradients in elastic modulus for improved contact-damage resistance. Part I: The silicon nitride–oxynitride glass system, Acta Mater. 49 (16) (2001) 3255–3262.
[12] S. Suresh, M. Olsson, A. Giannakopoulos, N. Padture, J. Jitcharoen, Engineering the resistance to sliding-contact damage through controlled gradients in elastic properties at contact surfaces, Acta Mater. 47 (14) (1999) 3915–3926.
[13] Y. He, K.-B. Yoo, H. Ma, K. Shin, Study of the austenitic stainless steel with gradient structured surface fabricated via shot peening, Mater. Lett. 215 (2018) 187–190.
[14] Q. Wang, Y. Yin, Q. Sun, L. Xiao, J. Sun, Gradient nano microstructure and its formation mechanism in pure titanium produced by surface rolling treatment, J. Mater. Res. 29 (4) (2014) 569–577.
[15] C. Ren, D. Wang, Q. Wang, Y. Guo, Z. Zhang, C. Shao, H. Yang, Z. Zhang, Enhanced bending fatigue resistance of a 50CrMnMoVNb spring steel with decarburized layer by surface spinning strengthening, Int. J. Fatigue 124 (2019) 277–287.
[16] W. Zhou, X. Ren, Y. Yang, Z. Tong, L. Chen, Tensile behavior of nickel with gradient microstructure produced by laser shock peening, Mater. Sci. Eng. A 771 (2020) 138603.
[17] J.-D. Kim, M.-H. Lee, S.-J. Lee, W.-J. Kang, Laser transformation hardening on rod-shaped carbon steel by Gaussian beam, Trans. Nonferr. Met. Soc. China 19 (4) (2009) 941–945.
[18] S. Su, L. Wang, R. Song, Y. Wang, J. Li, C. Chen, Gradient microstructure evolution and hardening mechanism of carburized steel under novel heat treatment, Mater. Lett. 280 (2020) 128486.
[19] C. Tromas, J.-C. Stinville, C. Templier, P. Villechaise, Hardness and elastic modulus gradients in plasma-nitrided 316l polycrystalline stainless steel investigated by nanoindentation tomography, Acta Mater. 60 (5) (2012) 1965–1973.
[20] T. Fang, W. Li, N. Tao, K. Lu, Revealing extraordinary intrinsic tensile plasticity in gradient nano-grained copper, Science 331 (6024) (2011) 1587–1590.
[21] Y. Wei, Y. Li, L. Zhu, Y. Liu, X. Lei, G. Wang, Y. Wu, Z. Mi, J. Liu, H. Wang, Evading the strength–ductility trade-off dilemma in steel through gradient hierarchical nanotwins, Nature Commun. 5 (1) (2014) 1–8.
[22] Z. Cheng, H. Zhou, Q. Lu, H. Gao, L. Lu, Extra strengthening and work hardening in gradient nanotwinned metals, Science 362 (6414) (2018).
[23] L. Yang, N. Tao, K. Lu, L. Lu, Enhanced fatigue resistance of Cu with a gradient nanograined surface layer, Scr. Mater. 68 (10) (2013) 801–804.
[24] J. Long, Q. Pan, N. Tao, M. Dao, S. Suresh, L. Lu, Improved fatigue resistance of gradient nanograined Cu, Acta Mater. 166 (2019) 56–66.
[25] Y. Zhang, Z. Han, K. Wang, K. Lu, Friction and wear behaviors of nanocrystalline surface layer of pure copper, Wear 260 (9–10) (2006) 942–948.
[26] N.A. Prakash, R. Gnanamoorthy, M. Kamaraj, Friction and wear behavior of surface nanocrystallized aluminium alloy under dry sliding condition, Mater. Sci. Eng. B 168 (1–3) (2010) 176–181.
[27] H. Wu, Y. Liu, X. Zhang, In-plane crushing behavior and energy absorption design of composite honeycombs, Acta Mech. Sinica 34 (6) (2018) 1108–1123.
[28] S. Wang, Z. Zheng, Y. Ding, C. Zhu, J. Yu, Dynamic crushing of cellular materials: a particle velocity-based analytical method and its application, Acta Mech. Sinica 35 (4) (2019) 839–851.
[29] S.R. Bates, I.R. Farrow, R.S. Trask, Compressive behaviour of 3D printed thermoplastic polyurethane honeycombs with graded densities, Mater. Des. 162 (2019) 130–142.

[30] X. Wu, Y. Su, J. Shi, In-plane impact resistance enhancement with a graded cell-wall angle design for auxetic metamaterials, Compos. Struct. 247 (2020) 112451.
[31] X. Zhang, H. Zhang, Optimal design of functionally graded foam material under impact loading, Int. J. Mech. Sci. 68 (2013) 199–211.
[32] H. Wu, X. Zhang, Y. Liu, In-plane crushing behavior of density graded cross-circular honeycombs with zero Poisson's ratio, Thin-Walled Struct. 151 (2020) 106767.
[33] Y. Nian, S. Wan, M. Li, Q.J.C. Su, B. Materials, Crashworthiness design of self-similar graded honeycomb-filled composite circular structures, Constr. Build. Mater. 233 (2020) 117344.
[34] Y. Nian, S. Wan, M. Li, Q. Su, Crashworthiness design of self-similar graded honeycomb-filled composite circular structures, Constr. Buil. Mater. 233 (2020) 117344.
[35] B. Yu, B. Han, P.-B. Su, C.-Y. Ni, Q.-C. Zhang, T.J. Lu, Graded square honeycomb as sandwich core for enhanced mechanical performance, Mater. Des. 89 (2016) 642–652.
[36] J.J. Andrew, J. Ubaid, F. Hafeez, A. Schiffer, S. Kumar, Impact performance enhancement of honeycombs through additive manufacturing-enabled geometrical tailoring, Int. J. Impact Eng. 134 (2019) 103360.
[37] C. Qi, F. Jiang, S. Yang, Advanced honeycomb designs for improving mechanical properties: A review, Composites B 227 (2021) 109393.
[38] L. Hu, M.Z. Zhou, H. Deng, Dynamic indentation of auxetic and non-auxetic honeycombs under large deformation, Compos. Struct. 207 (2019) 323–330.
[39] Z. Li, K. Wang, B. Wang, Indentation resistance of brittle auxetic structures: Combining discrete representation and continuum model, Eng. Fract. Mech. 252 (2021) 107824.
[40] T. Asada, Y. Tanaka, N. Ohno, Two-scale and full-scale analyses of elastoplastic honeycomb blocks subjected to flat-punch indentation, Int. J. Solids Struct. 46 (7–8) (2009) 1755–1763.
[41] J. Wan, J.-W. Jiang, H.S. Park, Machine learning-based design of porous graphene with low thermal conductivity, Carbon 157 (2020) 262–269.
[42] G.X. Gu, C.-T. Chen, M.J. Buehler, De novo composite design based on machine learning algorithm, Extreme Mech. Lett. 18 (2018) 19–28.
[43] P.Z. Hanakata, E.D. Cubuk, D.K. Campbell, H.S. Park, Accelerated search and design of stretchable graphene kirigami using machine learning, Phys. Rev. Lett. 121 (25) (2018) 255304.
[44] C.T. Chen, G.X. Gu, Generative deep neural networks for inverse materials design using backpropagation and active learning, Adv. Sci. 7 (5) (2020) 1902607.
[45] J. Newman, An Evaluation of Fracture Analysis Methods, in: Elastic–Plastic Fracture Mechanics Technology, ASTM International, Philadelphia, 1985.
[46] L. Xue, Damage accumulation and fracture initiation in uncracked ductile solids subject to triaxial loading, Int. J. Solids Struct. 44 (16) (2007) 5163–5181.
[47] K. Dai, J. Villegas, L. Shaw, An analytical model of the surface roughness of an aluminum alloy treated with a surface nanocrystallization and hardening process, Scr. Mater. 52 (4) (2005) 259–263.
[48] Z. Zhu, K. Guo, J. Sun, J. Li, Y. Liu, Y. Zheng, L. Chen, Evaluation of novel tool geometries in dry drilling aluminium 2024-T351/titanium Ti6Al4V stack, J. Mater Process. Technol. 259 (2018) 270–281.
[49] L.J. Gibson, M.F. Ashby, Cellular Solids : Structure and Properties, Cambridge University Press, Cambridge, England, 1997.
[50] A. Zunger, Inverse design in search of materials with target functionalities, Nature Rev. Chem. 2 (4) (2018) 1–16.
[51] J. Zhang, G. Lu, Z. Wang, D. Ruan, A. Alomarah, Y. Durandet, Large deformation of an auxetic structure in tension: Experiments and finite element analysis, Compos. Struct. 184 (2018) 92–101.
[52] A. Wei, J. Xiong, W. Yang, F. Guo, Deep learning-assisted elastic isotropy identification for architected materials, Extreme Mech. Lett. 43 (2021) 101173.
[53] W. Dai, Q. Yang, G.-R. Xue, Y. Yu, Boosting for transfer learning, in: Proceedings of the 24th International Conference on Machine Learning, 2007, pp. 193–200.
[54] J.C. Weaver, G.W. Milliron, A. Miserez, K. Evans-Lutterodt, S. Herrera, I. Gallana, W.J. Mershon, B. Swanson, P. Zavattieri, E. DiMasi, The stomatopod dactyl club: a formidable damage-tolerant biological hammer, Science 336 (6086) (2012) 1275–1280.
[55] Z. Wei, X. Xu, FEM simulation on impact resistance of surface gradient and periodic layered bionic composites, Compos. Struct. 247 (2020) 112428.
[56] A. Ajdari, H. Nayeb-Hashemi, A. Vaziri, Dynamic crushing and energy absorption of regular, irregular and functionally graded cellular structures, Int. J. Solids Struct. 48 (3–4) (2011) 506–516.
[57] J. Zhang, H. Wei, Z. Wang, L. Zhao, Dynamic crushing of uniform and density graded cellular structures based on the circle arc model, Lat. Am. J. Solids Struct. 12 (6) (2015) 1102–1125.
[58] L. Hu, M.Z. Zhou, H. Deng, Dynamic crushing response of auxetic honeycombs under large deformation: theoretical analysis and numerical simulation, Thin-Walled Struct. 131 (2018) 373–384.